Effects of high-flux low-energy ion bombardment on the low-temperature growth morphology of TiN(001) epitaxial layers

Brian W. Karr,* David G. Cahill, I. Petrov, and J. E. Greene

Department of Materials Science, the Materials Research Laboratory, and the Coordinated Science Laboratory, University of Illinois, Urbana, Illinois 61801

(Received 25 January 2000)

Ultrahigh vacuum scanning tunneling microscopy (STM) is used to characterize the surface morphology of TiN(001) epitaxial layers grown by dc reactive magnetron sputtering at growth temperatures of $T_s = 650$ and $T_s = 750\,°C$. An auxiliary anode is used to bias the N_2 plasma and produce a large flux of low-energy N_2^+ ions that bombard the film surface during growth: the ratio of the N_2^+ flux to the Ti growth flux is ≈ 25. At ion energies E_i near the threshold for the production of bulk defects ($E_i = 43\,eV$ and $T_s = 650\,°C$), ion bombardment decreases the amplitude of the roughness, decreases the average distance between growth mounds, and reduces the sharpness of grooves between growth mounds. The critical island radius for second layer nucleation R_c is approximately 12 and 17 nm at growth temperatures of 650 and 750 °C respectively; at 650 °C, R_c is reduced to $\approx 10\,nm$ by ion bombardment.

I. INTRODUCTION

In many cases of technological importance, crystalline thin films are deposited at relatively low temperatures: under these conditions the vapor pressure of the solid film is completely negligible in comparison to the growth flux, and the equilibrium areal density of adatoms and other surface point defects is also small compared to the adatom density created by the growth flux. Experiments, theory, and computational modeling have shown that the morphology of crystal surfaces grown in this low temperature regime is often intrinsically unstable.[1] Asymmetries in the kinetics of adatom attachment at steps drive a pattern formation for growth mounds.[2,3] The asymmetry can arise from a repulsive barrier for an adatom crossing a descending step, the Ehrlich-Schwoebel barrier,[4] from an attractive interaction at an ascending step,[5–7] or from barriers for the diffusion of adatoms along step-edges when crossing corner sites.[8,9]

For weak asymmetries in the interaction of adatoms with steps, many aspects of this pattern formation, e.g., the film thickness h and in-plane length scale d at the onset of roughening, can be understood based on a $(1+1)$-dimensional model of step motion.[10,11] This model has only one parameter: the ratio of the Ehrlich-Schwoebel length l_{ES}, a measure of the strength of the asymmetry, to the critical size of a terrace needed for the nucleation of a new layer of the crystal l_c. In the limit of a weak barrier $l_c/l_{ES} \gg 1$ and no thermal smoothing, mounds first appear at a film thickness of $h^* \approx (l_c/l_{ES})^2$ monolayers, and the distance between growth mounds at $h = h^*$ is $d \approx l_c (l_c/l_{ES})^{1/2}$. As we discuss below, the large size of growth mounds on TiN(001) is caused by the relatively large value of l_c for this surface.

Figure 1 summarizes some recent experiments[11–17] on the low-temperature growth morphology of crystals where both the height and the average separation between growth mounds has been measured either by diffraction or microscopy. The phenomenon is clearly general: growth mound morphologies have been observed during crystal growth of metals, semiconductors, and ceramics. The data in Fig. 1 do not illustrate how d and the surface width W evolve with film thickness but many systems show a power law coarsening $d \propto h^{1/4}$; regimes of more rapid[11] and weaker coarsening,[12,17] however, have also been observed.

Methods for ion-assisted film deposition—e.g., magnetron sputtering, plasma-assisted chemical vapor deposition, and ion-beam deposition—involve high fluxes of low-energy ions bombarding the growth surface.[18] Research directed at establishing a more fundamental understanding of this class of ''energetic processes'' at surfaces is a particularly active area of research on crystal growth physics. Ion bombardment has been shown to have dramatic influence on the nucleation of thin films on foreign substrates[19–24] and the suppression of
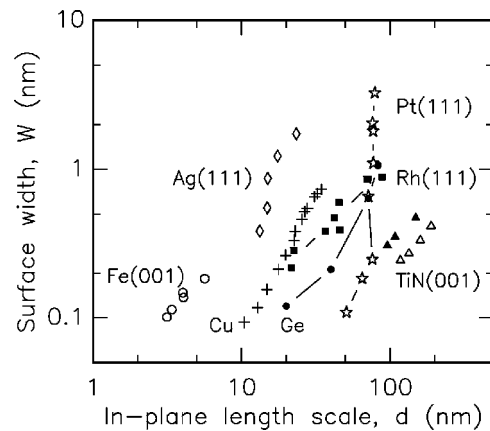

FIG. 1. Comparison of growth mound morphologies for Fe(001) (growth temperature 20 °C, Ref. 12), Ag(111) (200 K, Ref. 13), Cu(001) (30 °C, Ref. 15), Pt(111) (170 °C, Ref. 17), Rh(111) (450 °C Ref. 14), Ge(001) (155 °C, Ref. 11), and TiN(001) (open triangles, growth temperature 750 °C, Ref. 16; and filled triangles, 650 °C, this work). The surface width W is the rms roughness of the surface, and the in-plane length scale d is approximately equal to the average distance between growth mounds. In all cases, different data points correspond to different film thicknesses; in general, both W and d increase with increasing film thickness.

surface segregation in the growth of alloy films.[25] But well-controlled experiments on homoepitaxial crystal growth accompanied by low-energy ion bombardment have not been widely reported. Michely and co-workers studied nucleation rates and morphologies of Pt(111) grown by ion beam (400 and 4000 eV Ar$^+$) assisted evaporation[26] and ion beam sputter deposition.[27] The increased nucleation rates could be attributed to adatom clusters created by the relatively high ion energies used in Ref. 26, or by the backscattered noble gas atoms and the high-energy tail of sputtered Pt atoms.[27]

In this publication, we extend our previous work on TiN(001) growth morphology[16,28] to include the effects of high-flux low-energy ion bombardment at temperatures and ion energies near the threshold for the creation of bulk defects. We use scanning tunneling microscopy (STM) to measure the effects of ion bombardment on the evolution of the growth mound morphology and to determine the nucleation rate of islands on the relatively large terraces at the tops of growth mounds.

II. EXPERIMENTAL DETAILS

A. Substrate and buffer layer preparation

MgO(001) single crystals provide a nearly ideal substrate for the heteroepitaxial growth of TiN(001) (Ref. 29) because MgO and TiN have the same crystal structures (B1-NaCl) and nearly identical lattice constants at typical growth temperatures. The lattice mismatch is $\approx 0.2\%$ at 750 °C and $\approx 0.6\%$ at room temperature.[16] The increase in compressive stress after cooling from the growth temperature drives the extension of misfit dislocations and the appearance of slip steps[16] in some of the STM images shown below.

Polished MgO(001) substrates $10 \times 10 \times 0.5$ mm^3 are first prepared *ex situ* by annealing in air at 950 °C for 12 h; during annealing, the substrates are enclosed in a small, covered crucible of high-purity alumina. Atomic force microscopy, see Fig. 2(a), shows that surfaces of annealed MgO(001) crystals are atomically flat with large terraces, ~ 200 nm wide, separated by single and multiple atomic-height steps. In agreement with previous work,[30] annealing at higher temperatures produces rougher surfaces, presumably due to the thermal activation of bulk diffusion and surface segregation of impurities. Next, a 300 nm thick film of Mo is sputter deposited onto the back of the substrate to facilitate In-bonding of the substrate to a Mo sample block; the sample block and substrate are then degassed in the ultrahigh vacuum deposition chamber at 750 °C for 1 h. With the substrate at the growth temperature and before starting the N$_2$ gas flow, the chamber pressure is $\simeq 2 \times 10^{-8}$ mbar. Substrate temperatures are measured by a type-K thermocouple encased in a 0.8 mm diameter tube inserted into a 1 mm diameter $\times 1.6$ mm deep hole in the sample block.

The 99.999% pure 5 cm diam Ti target is sputtered in an atmosphere of purified N$_2$ at a pressure of 3.2×10^{-3} mbar. The target-to-sample distance is ≈ 20 cm. After deposition and cooling to room temperature, samples are transferred to the UHV STM analysis chamber without air exposure.[16]

Previously,[16,28] TiN epitaxial layers were deposited directly on MgO substrates at a growth temperature of 750 °C. Here, we first deposit a TiN buffer layer to provide a constant starting surface for subsequent TiN film growth: a pri-
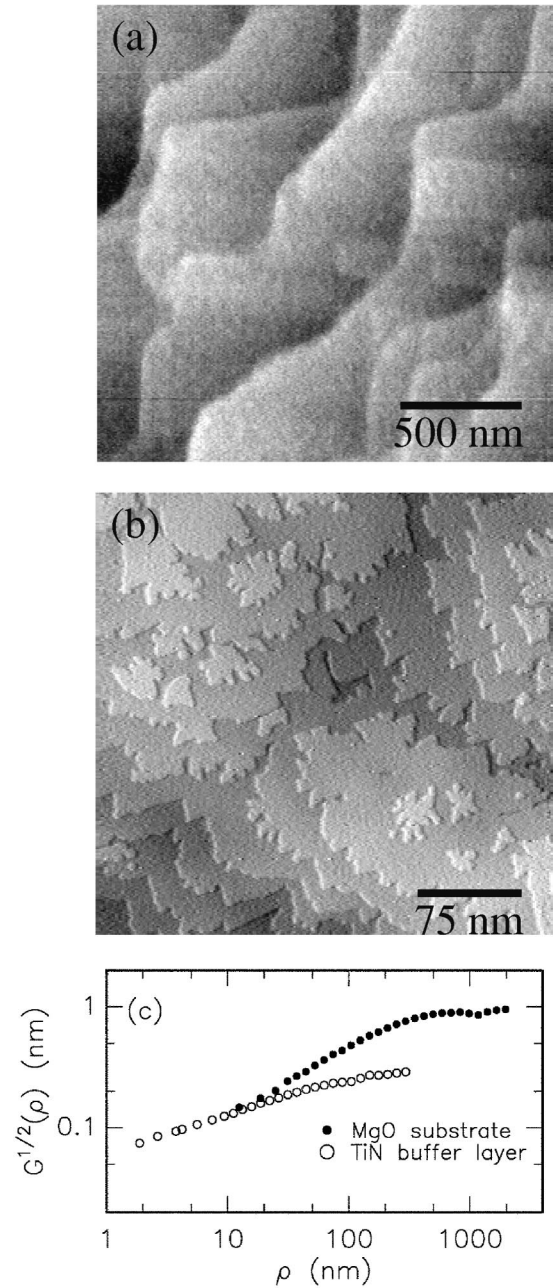

FIG. 2. (a) AFM image of the MgO(001) substrate surface after annealing in air at 950 °C for 12 h. The average height of the steps in this image is ~ 1 nm; i.e., most of the steps visible in this image are created by step-bunching of several atomic height steps. (b) STM image of a ~ 10 nm thick TiN(001) buffer layer grown on annealed MgO(001). The steps are one monolayer high, 0.21 nm. (c) Square root of the height difference correlation function for the two surfaces shown in (a) and (b).

mary goal of our research is to quantify the effects of ion bombardment on homoepitaxial crystal growth, and the buffer layer enables us to remove from our experiments the influence of ion bombardment on heteroepitaxial nucleation. We grow the buffer layer in two stages: a 10 nm layer of TiN at $T_s = 650$ °C and a growth rate of ≈ 1.6 nm min^{-1}, followed by 20 min deposition at 750 °C with the target power reduced by a factor of 10; this procedure is intended to create a high nucleation density of TiN on the MgO substrate followed by smoothing of the morphology using a reduced
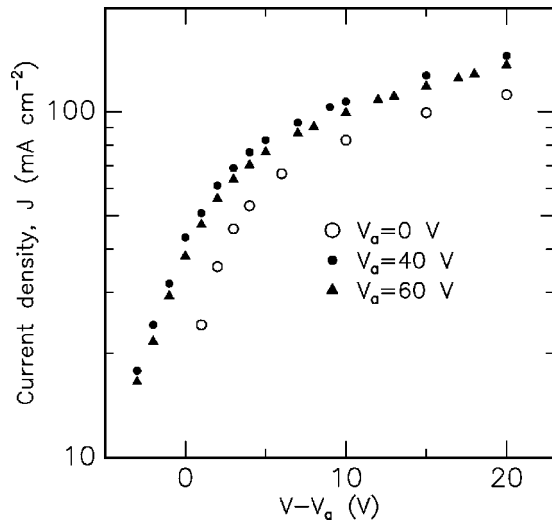
FIG. 3. Current density measured by a small diameter cylindrical Langmuir probe near the substrate position plotted as a function of the probe voltage V and the anode potential V_a.

growth rate at elevated temperature. The target current and voltage for deposition at 1.6 nm min^{-1} are 0.75 A, and 550 V, respectively. After the buffer layer is completed, a wire clip is adjusted by a sample manipulator to ensure that the buffer layer is electrically grounded for subsequent growths.

Figure 2(b) shows an STM image of a typical buffer layer; the array of atomic-height steps reflects the miscut of the underlying MgO crystal, $\approx 0.3°$. Height-difference correlation functions[31] $G(\rho)=\langle (h_i - h_j)^2 \rangle$ for the annealed MgO substrate and the TiN(001) buffer layer are shown in Fig. 2(c); h_i is the height of surface at point i, ρ is the distance between points i and j, and the brackets signify an average over many pairs of points i,j. At large ρ, $G^{1/2}(\rho)$ for the MgO substrate approaches 1 nm. This roughness is in good agreement with x-ray reflectivity measurements of the buried interface between a TiN buffer layer and the MgO substrate[28] indicating that growth of the buffer layer does not significantly disrupt the morphology of the MgO substrate. Buffer layer growth reduces the roughness of the starting surface by a factor of ~ 3 and also reduces the in-plane length-scale of the roughness by a factor of nearly 10, from ≈ 1000 to ≈ 100 nm.

B. Plasma biasing and characterization

We control the kinetic energy of ion bombardment by applying a positive bias voltage V_a to a 15 cm diameter ring-shaped anode placed between the target and substrate; the inside diameter of the ring is 8 cm. The composition of the ion flux during TiN sputtering was previously measured using double-modulation mass spectrometry.[33] In a 4×10^{-3} mbar N_2 plasma, N_2^+ is the dominant species and the ratios of $N_2^+ : N^+$, $N_2^+ : Ti^+$, and $N_2^+ : TiN^+$ are 28, 500, and 2×10^4, respectively. Most of the ions bombarding the surface are accelerated by the full sheath potential, $V_s = V_a + V_p$, where V_p is the plasma potential, because the mean-free-path for charge-exchange collision, ≈ 2 cm (Ref. 32) is larger than the sheath width w: $w \approx 1$ mm for $V_s = 80$ V and $w \approx 0.1$ mm for $V_s = 20$ V using the Child-Langmuir equation.[34]
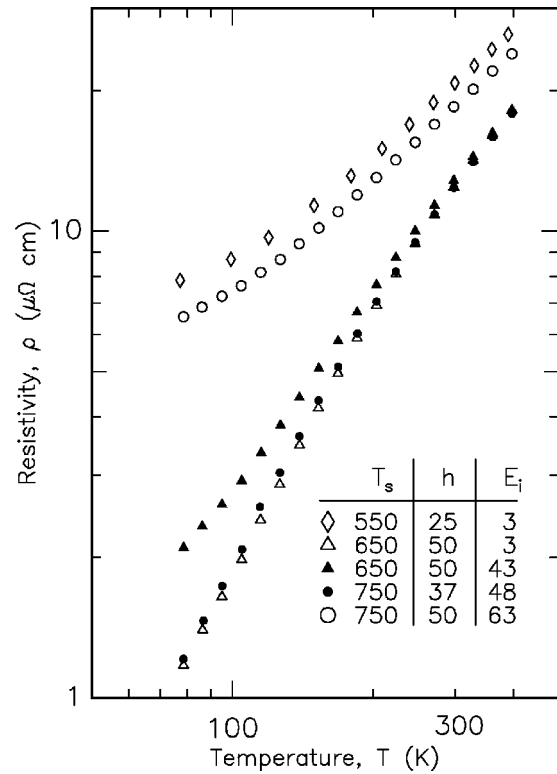

FIG. 4. Temperature dependence of the electrical resistivity of TiN(001) epitaxial films. Each data symbol is labeled by the growth temperature in °C, film thickness h in nm, and ion energy E_i in eV. $E_i = 43$ eV is near the threshold for bulk defect formation at a growth temperature of 650 °C; and the threshold is between 48 and 63 eV at a growth temperature of 750 °C. The lowest resistivity films have $\rho = 12.4 \mu\Omega$ cm at room temperature, 298 K.

We determine the ion flux F_i and sheath potential V_s using a cylindrical Langmuir probe constructed from a 0.25 mm diameter W wire with an exposed length of 5 mm.[35] Typical current-voltage curves are plotted in Fig. 3. Under these conditions, current collected by the Langmuir probe is dominated by electrons. The position of the knee in these data, $J_c = 0.08$ A cm^{-2} and $V - V_a = 3 \pm 1$ volts, gives an estimate of V_s and F_i:[35] $V_s = V_a + 3$ volts, and $F_i = 1.5(J_c/q)\sqrt{m_e/m_i} = 3.3 \times 10^{15}$ cm^{-2} sec^{-1}. The measured deposition rate is 1.6 nm min^{-1}; therefore, the Ti growth flux is 1.4×10^{14} cm^{-2} sec^{-1} and the ion flux F_i is a factor of ≈ 25 larger than the Ti growth flux.

C. Electrical properties

We use electrical resistivity to characterize the crystal quality of TiN, see Fig. 4. The room temperature resistivity is determined using a commercial four-point in-line probe combined with film thickness measurements by Rutherford backscattering spectroscopy and x-ray reflectivity. The highest quality films have a resistivity of 12.4 $\mu\Omega$ cm at room temperature. We measure the relative changes in the film resistivity as a function of temperature $77 < T < 400$ K using four-lead resistance measurements of an unpatterned film. For $E_i = 3$ eV ($V_a = 0$), and a growth temperature of $T_s = 650$ °C, the resistivity is controlled by the intrinsic electron-phonon scattering for $T > 77$ K. Lower temperature
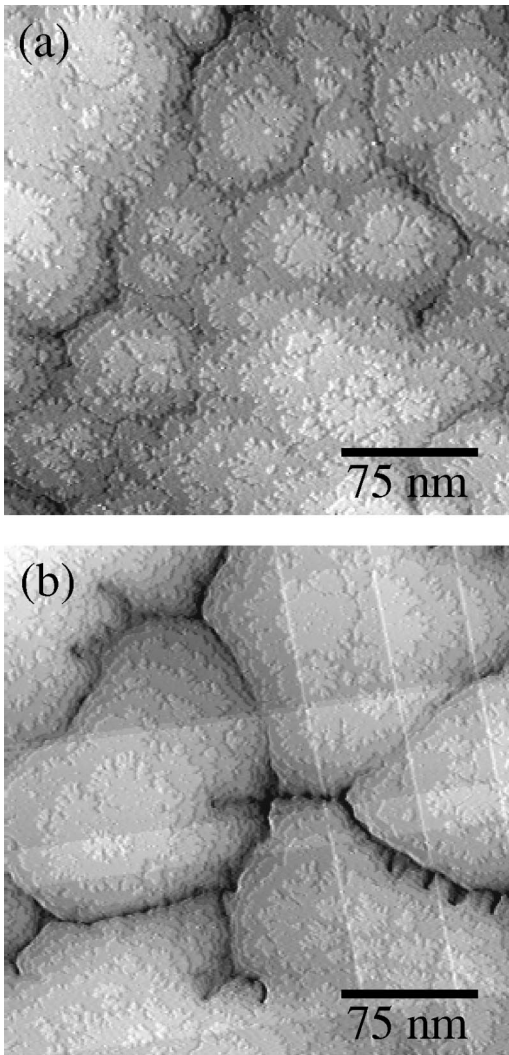
FIG. 5. STM images of TiN(001) films grown at 650 °C with $V_a=0$, i.e., $E_i \approx 3$ eV; (a) film thickness $h=16$ nm; (b) $h=140$ nm.

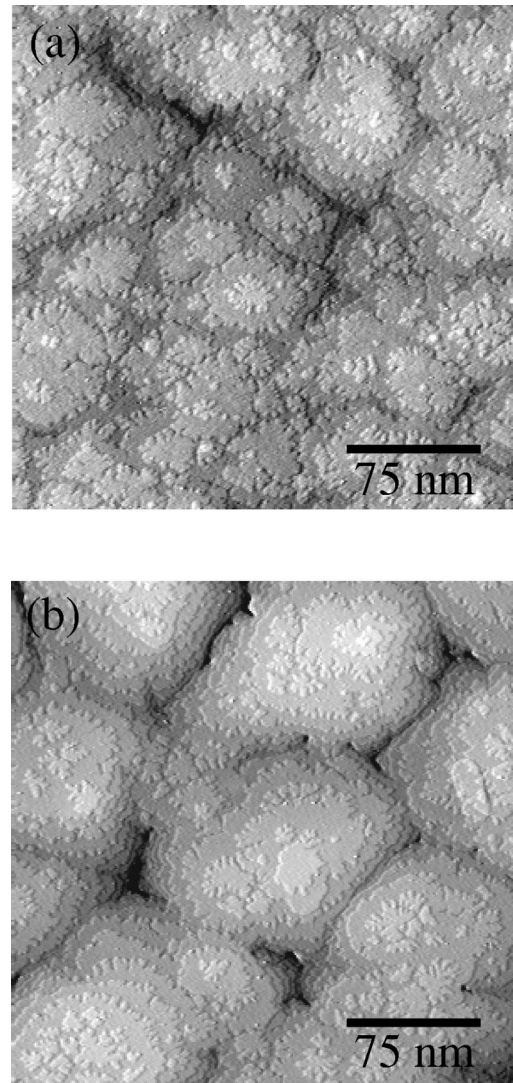
FIG. 6. STM images of TiN(001) films grown at 650 °C with $V_a=40$ volts, i.e., $E_i \approx 43$ eV; (a) film thickness $h=16$ nm; (b) $h=145$ nm.

deposition ($T_s=550$ °C) produces a large temperature-independent contribution to the resistivity of $\rho_0 \approx 7$ $\mu\Omega$ cm.

The threshold energy for ion-induced defects depends on the growth temperature: $E_i=43$ eV bombardment at $T_s=650$ °C produces a small increase in the resistivity of $\rho_0 \sim 1$ $\mu\Omega$ cm, and we conclude that this energy is close to the threshold energy for bulk defect formation at this temperature. (We do not know the nature or the concentration of the defects that are responsible for the excess electron scattering, but we note that radiation damage experiments using high-energy electron irradiation of Cu show that a 1 at. % concentration of Frenkel defects in Cu produces $\rho_0=2.8\mu\Omega$ cm.[36]) High-flux low-energy ion bombardment with $E_i=48$ eV at $T_s=750$ °C, however, does not create a measurable increase in the resistivity of TiN at 77 K, presumably because the healing of bulk-defects and transport of N interstitials is more rapid at this elevated temperature. The rapid healing of defects is not maintained for $E_i=63$ eV at $T_s=750$ °C; in this case, the residual resistivity is again relatively large, $\rho_0 \approx 6$ $\mu\Omega$ cm.

III. RESULTS AND DISCUSSION

A. Growth mound morphology

STM images of the growth morphology of TiN grown at 650 °C without and with high-flux low-energy ion bombardment are shown in Figs. 5 and 6, respectively. In all cases, the morphology is dominated by growth mounds; in general, the height and distance between growth mounds increases and grooves between growth mounds become increasingly well-defined with increasing film thickness. Ion bombardment creates subtle but measurable changes in the growth morphology.

We characterize these morphologies by two fundamental length scales: the in-plane length scale d and the amplitude of the surface roughness $A=G^{1/2}(d/2)$; $G(\rho)$ for the four surfaces shown in Figs. 5 and 6 are plotted as Fig. 7. We use the term ''roughness amplitude'' because $A \approx \sqrt{2}W$ where W is the rms roughness measured on a length scale comparable to d. Because of the relatively small surface roughness of these films, $A < 0.7$ nm, and because of residual long length-scale inhomogeneities in the morphology of the buffer layer,
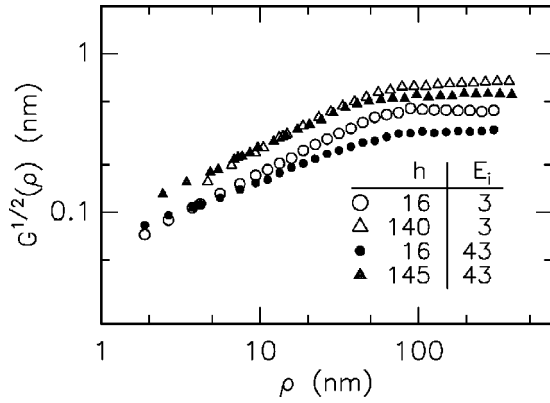
FIG. 7. Square root of the height difference correlation function for the four TiN(001) films shown in Figs. 5 and 6. Each data symbol is labeled by the film thickness h in nm and the ion energy E_i in eV.

we cannot routinely determine the in-plane length scale directly from statistical measurements of the surface roughness, e.g., a peak in the height-height correlation function[31] $H(\rho)=\langle h_i h_j \rangle$. Instead, we simply count the areal density of mounds n and set $d=n^{1/2}$; for this purpose, we define a growth mound as a local maximum of the surface height that is separated from neighboring mounds by a valley that is at least two monolayers deep.[16] In cases where a comparison can be made, we find that this measure for d is nearly identical to the position of the first peak in $H(\rho)$.

Figure 8 summarizes our results for the in-plane length scale d and roughness amplitude $A=G^{1/2}(d/2)$ for six films

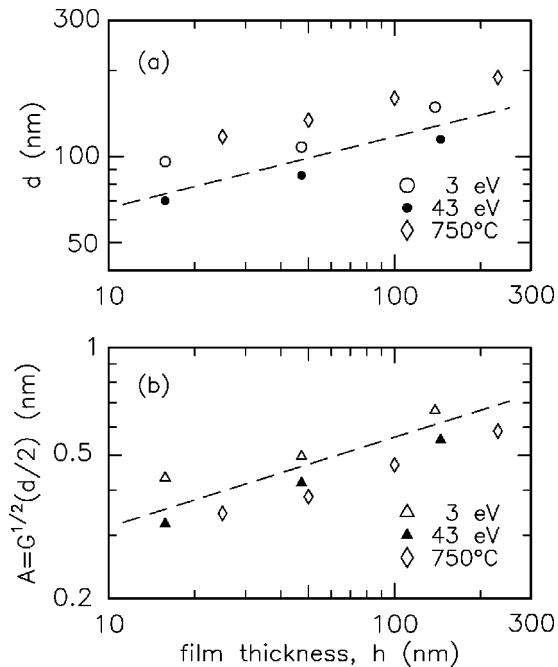
FIG. 8. Summary of (a) the in-plane length scale, d and (b) the roughness amplitude, $G^{1/2}(d/2)$ plotted versus film thickness h. The growth temperature is 650 °C; data symbols are labeled by the ion energy E_i. Data for growth at 750 °C on MgO(001) without the use of a TiN(001) buffer layer (Ref. 16) are shown as open diamonds. The dashed line shows a power law dependence of $h^{0.25}$ for comparison.
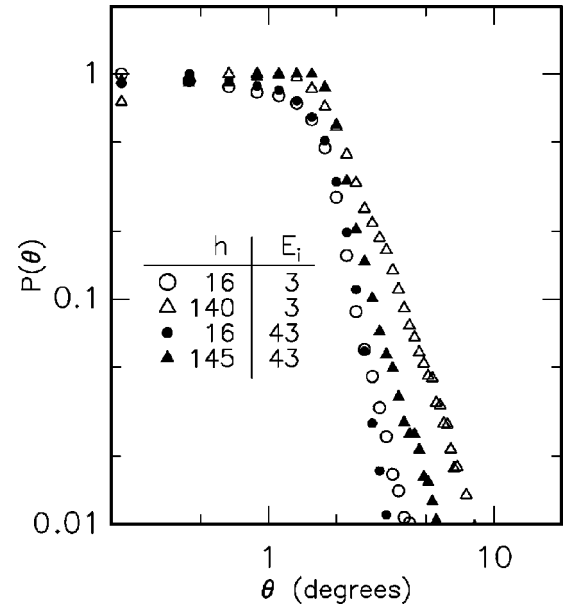

FIG. 9. Histogram of the the local surface slopes θ for the TiN(001) surfaces shown in Figs. 5 and 6. Data symbols are labelled by the film thickness h in nm and ion energy E_i in eV. The peak value of the probability distribution $P(\theta)$ has been set equal to unity in each case.

grown at 650 °C with comparison to our previous work on TiN(001) grown at 750 °C with $E_i=3$ eV.[16] These data show that the effects of ion bombardment and growth temperature are different: with no anode bias, i.e., $E_i=3$ eV, an increase in growth temperature from 650 to 750 °C increases d slightly and decreases A more significantly. This dependence of d and A on growth temperature has also been observed in the low-temperature growth of Ge(001).[11] An increase in E_i from 3 to 43 eV at 650 °C, on the other hand, causes d to decrease slightly while A also decreases.

These data for d and A show that ion bombardment has little effect on the average aspect ratio of the surface, i.e., A/d is essentially independent of ion energy E_i. The distribution of surface slopes, however, does depend on E_i, at least for thicker layers. This point is illustrated in Fig. 9 where we plot the probability distribution of surface orientations. Using an area of 4×4 nm^2 surrounding each image pixel, we calculate the local surface slope θ and create a histogram $P(\theta)$; the average orientation of the surface over a 400×400 nm^2 has been set to zero. For $h=140$ nm, ion bombardment suppresses the formation of large surface slopes: without ion bombardment, surface orientations associated with grooves between growth mounds extend to almost 10°; with $E_i=43$ eV, these angles are limited to $\approx6°$.

The data shown in Figs. 8 and 9 suggest that low-energy ion bombardment reduces the effective strength of the growth instability that drives the formation of growth mounds; i.e., the ratio (l_c/l_{ES}) is increased by ion bombardment. To get an estimate of (l_c/l_{ES}), we define the film thickness for the onset of growth mounds h^* as the film thickness at which the roughness amplitude is equal to 2 monolayers,[10,11] $A=0.42$ nm, and use $h^*\approx(l_c/l_{ES})^2$. Using these definitions, we find $(l_c/l_{ES})\approx12$, and ≈15 at $T_s=650$ °C and $E_i=3$ and 43 eV, respectively. For $T_s=750$ °C and $E_i=3$ eV, $(l_c/l_{ES})\approx18$.

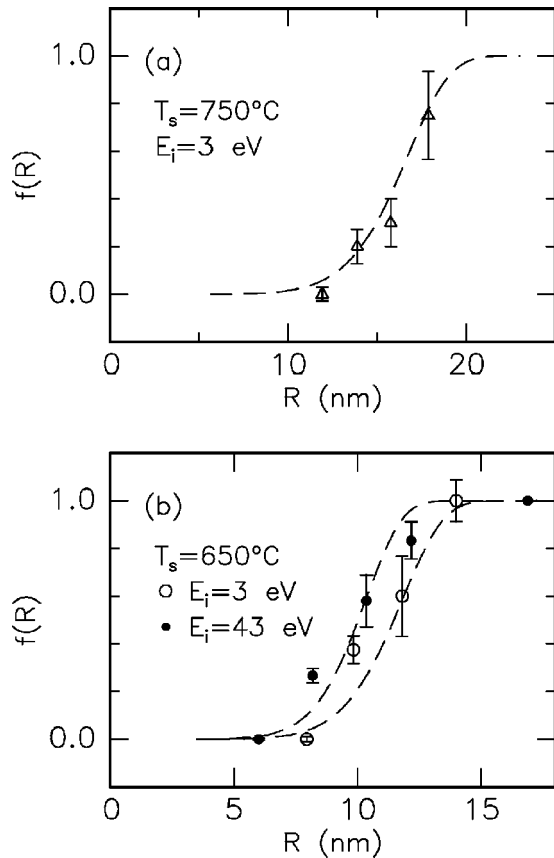FIG. 10. Fraction $f(R)$ of terraces with radius R that show nucleation of a new layer; (a) 750 °C, $E_i=3$ eV; (b) 650°, $E_i=3$ eV (open circles), and $E_i=43$ eV (filled circles). Error bars are an estimate of the statistical uncertainties in measuring $f(R)$. The dashed lines are fits to the data using $f(R)=1-\exp[-(R/R_c)^8]$ to determine the critical radius R_c for nucleation: (a) $R_c=17$ nm; (b) $R_c=12$ nm at $E_i=3$ eV, and $R_c=10.5$ nm at $E_i=43$ eV.

B. Nucleation of new layers

To gain a more microscopic perspective on the effects of ion bombardment on growth morphology, we analyze the STM images to extract the critical size of a terrace l_c that supports the nucleation of a new layer of the crystal. The growth mound morphology provides a relatively straightforward geometry for this analysis: nucleation occurs on the terraces at the tops of the growth mounds, and so we collect data on the sizes of these top terraces and statistics on the presence or absence of small islands that nucleate new layers. The top terraces are roughly elliptical with rough edges; we therefore measure the size of the terrace by drawing an ellipse within the rough boundary of the terrace. Since nucle-

ation on a highly elliptical terrace would be controlled by the length of the minor axis, we denote the minor radius of each top terrace by R. The critical terrace size l_c is then related to the critical radius R_c by $l_c \approx 2R_c$.

The fraction $f(R)$ of terraces of size R that show second-layer nucleation is plotted as Fig. 10. To facilitate a quantitative determination of R_c, we use the theoretical nucleation probability derived under the assumptions of circular terraces, weak step barriers, and a smallest stable island of two molecules;[37] and fit this theory to our data. By following this procedure, we do not require that these assumptions and the theory of Ref. 37 are a precise description of the physics of our growth experiments; the theoretical $f(R)$ simply provides a systematic method for determining R_c. We find $R_c=17$ nm at 750 °C and $R_c=12$ nm at 650 °C. These relatively large length scales for nucleation are responsible for the large size of growth mounds on TiN(001) in comparison to other materials systems, see Fig. 1. Ion bombardment creates a small shift of R_c to lower values, $R_c \approx 10$ nm, consistent with the reduction in the size of growth mounds d discussed above.

IV. CONCLUSIONS

We have measured the effects of low-energy ion bombardment on the growth morphology of TiN(001) using ultrahigh vacuum STM. A growth temperature of 650 °C and ion energy of 43 eV were chosen as the lowest possible temperature and highest possible ion energy compatible with the growth of high-quality, low-defect concentration TiN(001) epitaxial layers. With a ratio of N_2^+ flux to the Ti growth flux of ≈ 25, ion bombardment produces a small reduction in the roughness amplitude and the in-plane length scale of the growth mound morphology; the reduction in grooving at the boundaries between growth mounds is more pronounced. These results indicate that low-energy ion bombardment reduces the effective strength of the growth instability in this system. At a more microscopic level, ion bombardment produces a small decrease in the critical terrace size for nucleation of new layers; i.e., ion bombardment produces a small increase in the nucleation rate.

*Current address: Seagate Technology, Bloomington, Minnesota, 55435.

[1] Joachim Krug, Adv. Phys. **46**, 139 (1997); for a discussion of unstable MBE growth, see pp. 238–244.

[2] J. Villain, J. Phys. I **1**, 19 (1991).

[3] M.D. Johnson, C. Orme, A.W. Hunt, D. Graff, J. Sudijono, L.M. Sander, and B.G. Orr, Phys. Rev. Lett. **72**, 116 (1994).

[4] Gert Ehrlich and F.G. Hudda, J. Chem. Phys. **44**, 1039 (1966).

[5] Jacques G. Amar and Fereydoon Family, Phys. Rev. Lett. **77**, 4584 (1996).

[6] S.C. Wang and G. Ehrlich, Phys. Rev. Lett. **70**, 41 (1993).

[7] Kentaro Kyuno and G. Ehrlich, Surf. Sci. **383**, L766 (1997).

[8] O. Pierre-Louis, M.R. D'Orsogna, and T.L. Einstein, Phys. Rev. Lett. **82**, 3661 (1999).

[9] M.V. Ramana Murty and B.H. Cooper, Phys. Rev. Lett. **83**, 352 (1999).

[10] Paolo Politi and Jacques Villain, Phys. Rev. B **54**, 5114 (1996).

[11] Joseph E. Van Nostrand, S. Jay Chey, and David G. Cahill, Phys.

Rev. B **57**, 12 536 (1999).

[12] Joseph A. Stroscio, D.T. Pierce, M.D. Stiles, A. Zangwill, and L.M. Sander, Phys. Rev. Lett. **75**, 4246 (1995).

[13] W.C. Elliot, P.F. Miceli, T. Tse, and P.W. Stephens, Phys. Rev. B **54**, 17 938 (1996).

[14] F. Tsui, J. Wellman, C. Uher, and Roy Clark, Phys. Rev. Lett. **76**, 3164 (1996).

[15] J.-K. Zuo and J.F. Wendelken, Phys. Rev. Lett. **78**, 2791 (1997).

[16] Brian W. Karr, I. Petrov, David G. Cahill, and J.E. Greene, Appl. Phys. Lett. **70**, 1703 (1997).

[17] M. Kalff, P. Smilauer, G. Comsa, and T. Michely, Surf. Sci. **426**, L447 (1999).

[18] J.E. Greene in *Handbook of Crystal Growth*, edited by D.T.J. Hurle (Elsevier, New York, 1993), Vol. 1.

[19] C.-H. Choi, R. Ai, and S.A. Barnett, Phys. Rev. Lett. **67**, 2826 (1991).

[20] F. Adibi, I. Petrov, J.E. Greene, L. Hultman, and J.-E. Sundgren, J. Appl. Phys. **73**, 8580 (1993).

[21] L. Hultman, J.-E. Sundgren, J.E. Greene, D.B. Bergstrom, and I. Petrov, J. Appl. Phys. **78**, 5395 (1995).

[22] Y.-W. Kim, I. Petrov, H. Ito, and J.E. Greene, J. Vac. Sci. Technol. A **13**, 2836 (1995).

[23] Brian W. Karr, Y.W. Kim, I. Petrov, D.B. Bergstrom, David G. Cahill, J.E. Greene, L.D. Madsen, and J.-E. Sundgren, J. Appl. Phys. **80**, 6699 (1996).

[24] R.L. Headrick, S. Kycia, A.R. Woll, and M.V. Ramana Murty, Phys. Rev. B **58**, 4818 (1998).

[25] Gang He and Harry A. Atwater, Appl. Phys. Lett. **68**, 664 (1996).

[26] S. Esch, M. Breeman, M. Morgenstern, T. Michely, and G. Comsa, Surf. Sci. **365**, 187 (1996).

[27] Matthias Kalff, Marinus Breeman, Markus Morgenstern, Thomas Michely, and George Comsa, Appl. Phys. Lett. **70**, 182 (1997).

[28] B.W. Karr, I. Petrov, P. Desjardins, D.G. Cahill, and J.E. Greene, Surf. Coat. Technol. **94–95**, 403 (1997).

[29] L. Hultman, S.A. Barnett, J.-E. Sundgren, and J.E. Greene, J. Cryst. Growth **92**, 639 (1988).

[30] Abhijit B. Joshi and M. Grant Norton, Appl. Surf. Sci. **115**, 307 (1995).

[31] Jean Lapujoulade, Surf. Sci. Rep. **20**, 191 (1994); see pp. 197 and 235.

[32] R.F. Stebbing, B.R. Turner, and A.C.H. Smith, J. Chem. Phys. **38**, 2277 (1963).

[33] I. Petrov, A. Myers, J.E. Greene, and J.R. Abelson, J. Vac. Sci. Technol. A **12**, 2846 (1994).

[34] G. Chapman, *Glow Discharge Processes* (Wiley, New York, 1980).

[35] I. Petrov, V. Orlinov, I. Ivanov, and J. Kourtev, Contrib. Plasma Phys. **28**, 157 (1988); see also page 69 of Ref. 28.

[36] W.E. King and R.E. Benedek, Phys. Rev. B **23**, 6335 (1981).

[37] J. Tersoff, A.W. Denier van der Gon, and R.M. Tromp, Phys. Rev. Lett. **72**, 266 (1997).